Available online at www.sciencedirect.com
SCIENCE DIRECT
Thin Solid Films 514 (2006) 310–315
thin solid films
www.elsevier.com/locate/tsf

Carrier transport and optical properties in GaAs far-infrared/terahertz mirror structures

H.B. Ye, Y.H. Zhang, W.Z. Shen *

Laboratory of Condensed Matter Spectroscopy and Opto-Electronic Physics, Department of Physics, Shanghai Jiao Tong University, 1954 Hua Shan Road, Shanghai 200030, PR China

Received 30 May 2005; received in revised form 14 February 2006; accepted 6 March 2006
Available online 17 April 2006

Abstract

We report on detailed carrier transport and optical properties in doped/undoped GaAs far-infrared (FIR)/terahertz (THz) mirror structures for GaAs-based FIR/THz device application. By the aid of variable magnetic field Hall and Shubnikov de Haas measurements, we have analyzed the carrier concentration, mobility and scattering times. It is found that ionized impurity scattering is the dominant scattering mechanism in the GaAs FIR/THz mirror structures. We investigate numerically the energy flux along the mirror depth and the reflection of the mirror structure. The experimental FIR/THz reflection and transmission spectra demonstrate the reliability of the optical analysis.

PACS: 42.79.Fm; 85.60.Bt; 78.30.Fs; 72.20.Fr; 72.80.Ey
Keywords: Optoelectronic devices; Electrical properties and measurements; Optical properties; Molecular beam epitaxy (MBE)

1. Introduction

Far-infrared (FIR)/terahertz (THz) electromagnetic radiation and detection have received more and more attention nowadays, due to their potential applications in various areas, such as biomedical imaging, quantum computing, space astronomy, spectroscopy, and communications [1–4]. The typical examples of FIR/THz semiconductor devices with mature GaAs material are quantum cascade lasers (QCLs) [5] and homojunction internal photoemission FIR detectors [6]. It is well known that resonant-cavity-enhanced (RCE) structures have been widely employed to improve the performance of semiconductor devices. The RCE structures are simply formed by sandwiching devices between a pair of mirrors, and proper design of these mirrors (or reflectors) is essential. Previous reports on the application of resonant cavities concentrate mainly on the near- and mid-infrared semiconductor devices [7], where distributed Bragg reflectors (DBRs) have shown excellent effect and structure popularity.

Nevertheless, there is little discussion about the RCE structures for FIR/THz semiconductor devices. Due to the long wavelength and free carrier absorption nature in the FIR/THz region, it is much more complex to design FIR/THz mirrors, in comparison with the near- and mid-infrared counterparts. The following three conditions should be considered simultaneously: (i) the mirror materials must be well lattice-matched to avoid the introduction of defects into the device layers; (ii) the mirrors should have high reflectivity and well-matched phase; and (iii) the performance of the RCE scheme depends critically on the realization of a low loss mirror. Recently, we have proposed a RCE structure for GaAs homojunction FIR detectors [8]. The top mirror of the RCE structure is a native semiconductor/air interface for simplicity and the bottom mirror consists of doped/undoped GaAs multilayers. Such doped/undoped GaAs FIR/THz mirror structures have demonstrated a satisfactory effect. The resulting quantum efficiency in the GaAs FIR detector cavity is three times of the normal one without the RCE structure [9].

The better understanding of the doped/undoped GaAs FIR/THz mirrors is helpful for the application of such a mirror concept in other kinds of GaAs-based FIR/THz semiconductor devices, taking advantages of the mature and uniform material

* Corresponding author. Fax: +86 21 54743242.
E-mail addresses: yuehzhang@sjtu.edu.cn (Y.H. Zhang), wzshen@sjtu.edu.cn (W.Z. Shen).

0040-6090/$ - see front matter © 2006 Elsevier B.V. All rights reserved.
doi:10.1016/j.tsf.2006.03.009

as well as monolithic integration technology. The potential application includes the extension of vertical-cavity surface emitting QCLs [10] to FIR/THz region with GaAs. In this paper, we have carried out a detailed electrical and optical investigation on this kind of doped/undoped GaAs FIR/THz mirror structure. Through variable magnetic field Hall and Shubnikov de Haas (SdH) measurements, we obtain the information of carrier concentration, mobility and scattering times. The energy flux along the mirror depth and the reflection of the mirror structure have been investigated numerically, and experimental FIR/THz reflection and transmission spectra are measured to verify the reliability of the optical analysis.

2. Experimental details

The doped/undoped GaAs multilayer FIR/THz mirror structures were grown by molecular beam epitaxy (MBE) on semi-insulating GaAs substrates [9]. The sample consists of three GaAs layers: a highly doped top layer (n doped by Si, 2×10^{18} cm^{-3}) with a thickness of 3000 Å followed by an intrinsic undoped layer (1.45 μm) and a thick highly doped bottom layer (1.80 μm, n doped by Si, 3×10^{18} cm^{-3}). The magnetic field dependent Hall and SdH measurements were performed in the Van der Pauw configuration by a set of Keithley Hall measurement system, including a 220 programmable current source, 2182 nanovoltmeter and 7001 switch system with a 7065 Hall card [11]. The ohmic contacts were fabricated by alloying indium on the surface of the GaAs multilayer structure. The sample was immersed in a ^{4}He cryostat system equipped with a 15 Tesla Oxford Instruments superconductive magnet, where the measured temperature can be down to 1.6 K. The magnetic field reading accuracy was better than 1%. The FIR/THz reflection and transmission spectra were performed on a Nicolet Nexus 870 Fourier transform infrared spectrometer with a deuterated triglycine sulfate (DTGS) polyethylene detector, solid substrate beamsplitter and infrared globar source. The reflection measurements were taken with near-normal incidence geometry (less than 10° incidence angle). The optical measurements were made with a resolution of 2.0 cm^{-1}.

3. Results and discussion

3.1. Magnetic field dependent hall effect

Fig. 1(a) presents the magnetic field (B) dependence of the experimental results (scatters) at 6.0 K, in the form of conductivity components $\sigma_{xx}(B)$ and $\sigma_{xy}(B)$, for the doped/undoped GaAs FIR/THz mirror structure. Here the variable magnetic field Hall measurements were performed in the magnetic field range from 0 to 7 Tesla because of the presence of the SdH oscillations at higher magnetic fields. The experimental fact that we have observed negative values of $\sigma_{xy}(B)$ throughout the magnetic field reflects the n-type nature of the measured sample, which is in agreement with our MBE design of the FIR/THz mirror structure. It should be noted that traditional fixed magnetic field Hall measurements only give average carrier concentration and mobility. In combination with mobility spectra analysis (MSA) procedures [12], the variable magnetic field Hall measurements, as shown in Fig. 1(a), can yield the distribution of electron mobility and extract the transport parameters of all carrier species present within the sample that are contributing to the conducting processes [11–13].

In the MSA approach, discrete carriers are generalized by a conductivity concentration function which spreads over a continuous mobility (μ) range. The two conductivity tensors are given by [12]:

$$\sigma_{xx}(B)=\frac{\rho(B)}{\rho^2(B)+B^2R_H^2(B)}=\int_0^\infty\frac{s^p(\mu)+s^n(\mu)}{1+\mu^2B^2}\mathrm{d}\,\mu$$
$$\sigma_{xy}(B)=\frac{BR_H(B)}{\rho^2(B)+B^2R_H^2(B)}=\int_0^\infty\frac{(s^p(\mu)-s^n(\mu))\mu B}{1+\mu^2B^2}\mathrm{d}\,\mu \quad (1)$$

where $R_H(B)$ and $\rho(B)$ are the experimental magnetic field dependent Hall coefficient and resistivity, respectively, and $s^p(\mu)$ and $s^n(\mu)$ are the hole and electron conductivity concentration functions, respectively. The MSA would transform the above experimental magnetic field dependent Hall data into the dependence of the conductivity concentration function on the mobility, in which each kind of carrier contributing to the total conductivity appears as a separate peak at a given mobility. Fig. 1(b) shows the corresponding mobility spectrum obtained via the MSA procedures from the experimental $\sigma_{xx}(B)$ and $\sigma_{xy}(B)$. The solid curves in Fig. 1(a) are the calculated $\sigma_{xx}(B)$ and $\sigma_{xy}(B)$ obtained using the carrier concentrations and mobility distributions in Fig. 1(b), which show good agreement with the experimental data.

In Fig. 1(b), there is only one electron peak in the mobility spectrum by the MSA, revealing only one electron species there. This is reasonable, since there is only one kind of n-type high doping concentration ($2–3\times10^{18}$ cm^{-3}) in the studied GaAs FIR/THz mirror structure. The peak corresponds to an effective value of the highly doped GaAs layers, which dominate the conductivity. The contributions of the undoped GaAs layer and semi-insulating GaAs substrate to the

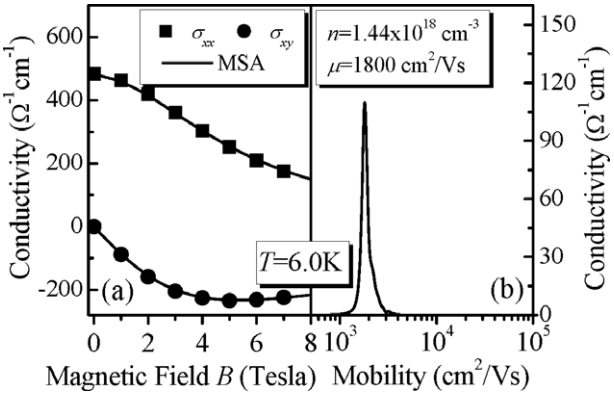

Fig. 1. (a) Experimental conductivity tensor components $\sigma_{xx}(B)$ and $\sigma_{xy}(B)$ as a function of magnetic field B for the doped/undoped GaAs multilayer FIR/THz bottom mirror structure at 6.0 K. The solid curves are the calculated results by using MSA procedures. (b) The yielded mobility spectrum.

conductivity can be ignored. Since the measured conductivity data are related to the total thickness of the three GaAs layers, the yielded Hall density of 1.44×10^{18} cm^{-3} is the average concentration of all the three layers in the sample. In fact, if we subtract the 1450 nm intrinsic layer, we can obtain the Hall density of 2.43×10^{18} cm^{-3} for the two highly doped GaAs layers. The electron mobility value of 1800 cm^2/Vs is quite consistent with the previously reported result of ~ 2000 cm^2/Vs for the same doping level of *n*-GaAs [14]. The narrow distribution of the mobility demonstrates the good doping uniformity of the sample.

3.2. Shubnikov de Haas oscillations

The SdH effect has been accepted as a powerful tool for characterizing a wide variety of semiconductors and their properties, such as the carrier concentrations, scattering times, and effective masses. Well-resolved SdH oscillations have been observed on longitudinal magnetoresistance R_{xx} of the doped/undoped GaAs FIR/THz mirror structure at low temperatures (see Fig. 2). The observed one period SdH oscillations indicate single carrier species present in the FIR/THz mirror structure, which agrees with the above results of the variable magnetic field Hall measurements. It should be noted that the conditions for observing the SdH oscillations are [15]: (i) degeneracy of the electron gas, $E_F \gg k_BT$; (ii) low electron effective mass and low temperature, $\hbar\omega_c < E_F$ and $\hbar\omega_c > k_BT$; and (iii) high electron mobility, $\mu B > 1$, with E_F and $\omega_c = eB/m^*$ the zero-field Fermi energy and cyclotron frequency, respectively. The clear observation of the SdH oscillations at magnetic fields of 8–15 Tesla in Fig. 2 indicates the excellent quality of the mirror structure.

For the longitudinal resistivity ρ_{xx} case, we can employ the following expression to describe the relationship between the SdH oscillations and the parameters characterizing the material [16]:

$$\frac{\Delta\rho}{\rho_0} = \sum_{R=1}^{\infty} \frac{5}{2}\left(\frac{RP}{2B}\right)^{1/2} \frac{\beta Tm'\cos(R\pi\nu)}{\sinh(R\beta Tm'/B)} e^{-R\beta T_D m'/B} \cos 2\pi\left(\frac{R}{PB} - \frac{1}{8} - R\gamma\right) \tag{2}$$

where $\Delta\rho$ is the deviation of ρ_{xx} from the non-oscillatory background resistivity, ρ_0 is the zero-field resistivity, R is the index of summation in the Fourier series, $\beta = 2\pi^2 k_B m_0/\hbar e$ is a collection of constants, $P = \hbar e/E_F m^*$ is the SdH period, $m' = m^*/m_0$, ν is the spin splitting factor related to the effective g factor g^* by $\nu = m'g^*/2$, $T_D = \hbar/2\pi k_B\tau_q$ is the Dingle temperature with τ_q the quantum scattering time, and γ is the Onsager phase factor. Usually, the first term, $R = 1$, suffices to describe the temperature dependence of the amplitude. Eq. (2) is a generalization of the Adams and Holstein relation that includes the effects of a nonparabolic band and spin splitting [17].

The solid curves in Fig. 2 are the theoretical calculation of the low-temperature SdH oscillations. The carrier concentration n can be obtained from the frequency F of the SdH oscillations (periodic in $1/B$) through the relation of $F = \hbar(3\pi^2 n)^{2/3}/2e$. The quantum scattering time τ_q is deduced from the Landau level shape damping term of $\exp(-2\pi^2 k_B T_D m^*/\hbar eB)$. The effective mass m^* is obtained from the temperature damping term $X/\sinh(X)$ with $X = 2\pi^2 k_B T m^*/\hbar eB$, and is found to be a constant (independent of temperature) of $0.067m_0$ during the fitting procedures. The good agreement between the theoretical calculation and the experimental data in Fig. 2 reveals the sample's carrier concentration of 2.466, 2.395, 2.475, and 2.470×10^{18} cm^{-3}, and quantum scattering time of 0.0354, 0.0376, 0.0406, and 0.0383 ps for the temperature of 1.6, 2.5, 3.5, and 6.0 K, respectively. It should be noted that the yielded carrier concentration of ~ 2.4×10^{18} cm^{-3} from the SdH oscillations is related to the two highly doped layers, since the 1450 nm intrinsic layer does not satisfy the second condition for observing the SdH oscillations. An evaluation at the same temperature of 6.0 K clearly demonstrates the good agreement between the SdH density (2.470×10^{18} cm^{-3}) and the above Hall one (2.43×10^{18} cm^{-3}).

As we know, the quantum scattering time (single-particle relaxation time) τ_q is sensitive to all scattering angles with all scattering events contributing with equal weight to the broadening of the Landau levels. There is another characteristic scattering time, the classical scattering time (transport lifetime) τ_c, which is dominated by large angle scattering events. The two characteristic scattering times are not equal ($\tau_c/\tau_q \approx 1$ only for isotropic scattering events with no angular preference). The ratio τ_c/τ_q is very useful in determining which scattering mechanism is dominant in limiting the mobility. If the dominant scattering process has strong angle dependence, the ratio τ_c/τ_q is much larger than unity. The classical scattering time can be directly obtained from the low-temperature Hall mobility via the Drude relation of $\tau_c = m^*\mu_H/e = 0.0686$ ps. As a result, the ratio of classical to quantum scattering time is 1.79 for the present sample at 6.0 K, which is larger than unity. At the low temperatures, at which we measure the scattering times, both acoustic and optical phonon modes of scattering are frozen out and the charges from any unintentional background donors are frozen onto the donor sites, rendering them neutral. The ratio of classical to quantum

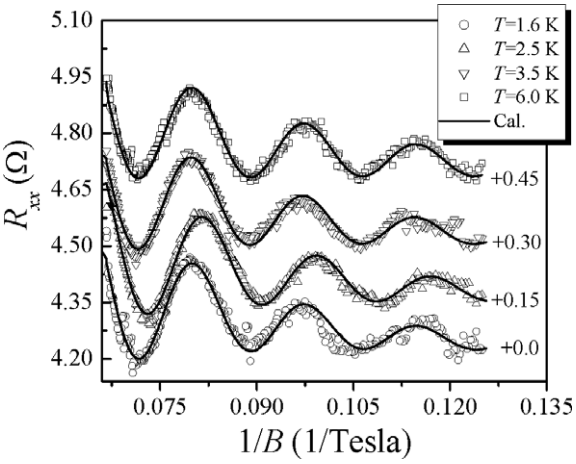

Fig. 2. Experimental (scatters) and calculated [solid curves, from Eq. (2)] longitudinal magnetoresistance R_{xx} as a function of $1/B$ for the doped/undoped GaAs multilayer FIR/THz bottom mirror structure at different temperatures of 1.6, 2.5, 3.5, and 6.0 K. The curves have been shifted by 0.15 Ω for clarity.

scattering time due to charged dislocation scattering in a degenerate three-dimensional electron system is given by [18]

$$\frac{\tau_{\mathrm{disl}}^{c}}{\tau_{\mathrm{disl}}^{q}} = 1 + 2k_{\mathrm{F}}^{2}\lambda_{\mathrm{TF}}^{2} \tag{3}$$

where $k_F=(3\pi^2 n)^{1/3}$ is the Fermi wave vector and $\lambda_{\mathrm{TF}}^2=2\varepsilon_0\varepsilon_\infty E_F/3e2n$ is the Thomas–Fermi screening length with ε_∞ the background dielectric constant. The ratio, which depends only on the carrier concentration for a degenerate electron system, is evidently greater than unity, and is found to be 7.6 for our sample, much larger than what we have observed. So we exclude charged dislocation scattering to be the most important scattering mechanism. Since the charged dislocation scattering is inherently more anisotropic than the ionized impurity scattering, the ratio due to ionized impurity scattering is expected to be much smaller than the one caused by charged dislocation scattering [18]. A quantum scattering time of 0.0392 ps due to ionized impurity scattering can be calculated in the mass-shell approximation [19]. Therefore we can identify unambiguously ionized impurity scattering as the dominant scattering mechanism at low temperatures for the GaAs FIR/THz mirror structure.

3.3. Calculation of energy flux, reflection and transmission

In the following, we will investigate the optical properties of the doped/undoped GaAs FIR/THz mirror structure. We first calculate the energy flux, the reflection and transmission spectra of the structure, and then demonstrate experimentally in Sec.3.4. The Fresnel matrix method is used to calculate complex reflection and/or absorption of multilayer medium [20,21]. In our model, one simplification is made that the light is normally incident without considering any light polarization effects. We label the medium from the top (the medium lying above the mirror structure) to the bottom (substrate) consequently as 0th, 1st, 2nd and so on. According to the Maxwell equations and the boundary conditions for the electrical vector continuity, the electric field at the jth layer can be simply expressed in terms of the $(j+1)$th layer:

$$\begin{pmatrix} E_j^+ \\ E_j^- \end{pmatrix} = \frac{1}{2}\begin{pmatrix} \left[1+\frac{\tilde{n}_{j+1}}{\tilde{n}_j}\right]e^{-i\delta_{j+1}} & \left[1-\frac{\tilde{n}_{j+1}}{\tilde{n}_j}\right]e^{i\delta_{j+1}} \\ \left[1-\frac{\tilde{n}_{j+1}}{\tilde{n}_j}\right]e^{-i\delta_{j+1}} & \left[1+\frac{\tilde{n}_{j+1}}{\tilde{n}_j}\right]e^{i\delta_{j+1}} \end{pmatrix}\begin{pmatrix} E_{j+1}^+ \\ E_{j+1}^- \end{pmatrix} \tag{4}$$

with $\delta_{j+1}=\frac{2\pi\tilde{n}_{j+1}}{\lambda}d_{j+1}$, where subscript j and $j+1$ denote the layer order. λ is the wavelength in the vacuum. $\tilde{n}$ is the respective complex refractive index and can be obtained from the following equation [22]:

$$\tilde{n}^2 = \tilde{\varepsilon} = \varepsilon_\infty\left[1-\frac{\omega_p^2}{\omega(\omega+i\omega_0)}\right] + \frac{\omega_{\mathrm{TO}}^2(\varepsilon_s-\varepsilon_\infty)}{\omega_{\mathrm{TO}}^2-\omega^2-i\gamma_p\omega} \tag{5}$$

with $\omega_p=(ne^2/\varepsilon_0\varepsilon_\infty m^*)^{1/2}$ the plasma frequency related with carrier concentration n and the electron effective mass m^*, $\omega_0=1/\tau$ the free-carrier damping constant, τ is carrier relaxation time, ε_s the low frequency dielectric constant of an intrinsic semiconductor, ω_{TO} the frequency of transverse optical (TO) phonons and γ_p the damping coefficient with dimension of frequency. For n-GaAs, $\hbar\omega_{\mathrm{TO}}=33.25$ meV, $\varepsilon_s=12.85$, $\varepsilon_\infty=10.88$, $\hbar\gamma_p=0.25$ meV, and $\tau=5.71\times10^{-14}+2.23\times10^{-14}\exp(-n/7.62\times10^{16})$ s [9]. With an initial value E_{j+1}^+ and E_{j+1}^- (e.g., $E_{j+1}^+=1$, $E_{j+1}^-=0$ for the substrate, which represents the final medium where only the transmitted optical wave exists. The initial value of E_{j+1}^+ could be chosen randomly which would not change the calculation results.), we can obtain the electric field (E_j^+,E_j^-), then (E_{j-1}^+,E_{j-1}^-) and more by repeating the same step of calculation. Then, all the real light field distributions $(E_j^+,E_j^-, j=0, 1, 2...)$ of the whole multilayer system are entirely determined, and consequently, the power reflectivity R and transmission T can be easily obtained.

The calculation of energy flux provides a direct and clear approach to investigate the absorption in each layer within the multilayer mirror structure, which helps to design low photon absorption of the mirror itself. Fig. 3 shows the ratio of energy flux to the incident optical energy from the highly doped top layer to the highly doped bottom layer of the mirror structure at four different wavelengths. Because the mirror structure is impossible to face the air directly in practice, the medium lying above the mirror structure is not air but a certain layer that the mirror structure is linked. For the present mirror structure, which is designed for the homojunction FIR detectors [6,8,9], incident medium of the mirror structure is a GaAs layer with a doping concentration of 10^{17} cm^{-3}. We have marked different medium from top to the bottom consequently with numbers (0 is the doped GaAs layer with the concentration of 10^{17} cm^{-3}, 1–4 is the mirror structure) in Fig. 3 and defined the depth at the interface where the light enters into the mirror structure to be 0 μm.

The decrease in the magnitude of the energy flux along the depth describes the absorption of each layer and the slope of the curve gives the efficiency of the absorption. From Fig. 3, it is clear that most of the absorption of the mirror structure falls inside the highly doped bottom layer. And the absorption in the highly doped top and intrinsic layers can be nearly ignored in contrast to the highly doped bottom layer. Due to the low carrier

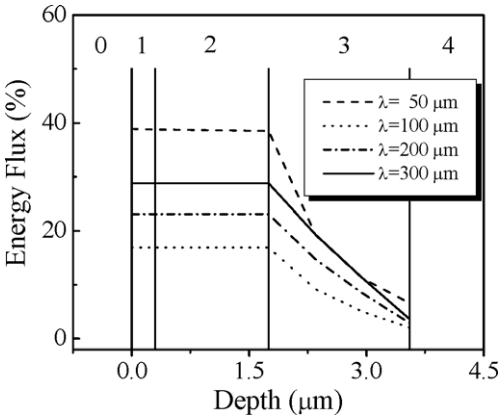

Fig. 3. The ratio of energy flux distribution to the incident optical energy along the depth from the highly doped top layer to the highly doped bottom layer of the GaAs mirror structure at different wavelengths. 0 denotes a GaAs layer with the doped concentration of 10^{17} cm^{-3}, 1–4 represent the highly doped top layer, intrinsic layer, highly doped bottom layer, and the semi- insulating GaAs substrate, respectively.

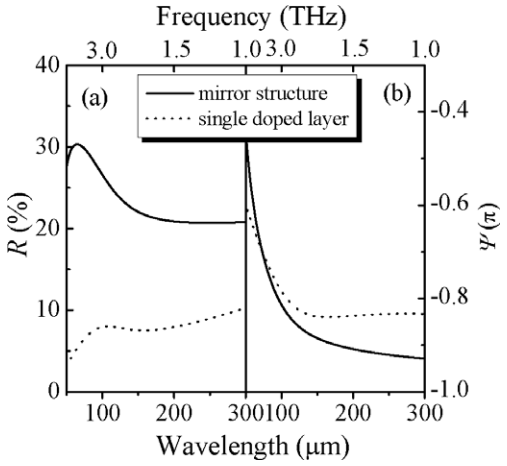

Fig. 4. The reflection (a) and the phase (b) of the GaAs FIR/THz mirror structure and a single doped GaAs layer (0.3 μm, 2×10^{18} cm^{-3}). The medium from which the light enters into the mirror structure is a doped GaAs layer with a doping concentration of 10^{17} cm^{-3}.

concentration, the negligible absorption in the intrinsic layer is easy to be understood. However, even though the carrier concentration is similar to that of the doped bottom layer, the absorption efficiency in the highly doped top layer is much lower than that of the doped bottom layer. This is because it is too thin (0.3 μm, compared to the thickness of 1.8 μm for the doped bottom layer) to affect the total optical field distribution, which can be controlled by changing the structural parameters (thickness and doping concentration) of each layer in the mirror structure. The abnormality of the 50 μm case in Fig. 3 compared with other three wavelengths results from the fact that it is close to the TO phonon band of GaAs.

Generally, the reflection is one of the most important parameters to characterize the performance of mirror structures. Fig. 4(a) shows the calculated reflection of the FIR/THz mirror structure (solid curve). Similar to the case of Fig. 3, the medium for the optical entrance is the doped GaAs layer with the doping concentration 10^{17} cm^{-3}. We note that the reflection in the entire wavelength/frequency region is much lower than traditional near- and mid-infrared DBRs whose reflectivity is usually higher than 90% [7]. The highest reflectivity is only 30.3%. This is because there exists free carrier absorption in FIR/THz region and the absorption of the mirror structure results in the reduction of the reflection inevitably. Nevertheless, the present mirror structure still shows clear enhancement of the reflection in the entire FIR/THz region, in comparison with the reflection of a single doped layer [the dotted curve in Fig. 4(a), normally the device contact layer] with the same thickness and doping concentration as the highly doped top layer of the mirror structure. In addition to the high amplitude reflectivity, a well-matched phase is required for the mirror structure. In Fig. 4(b), we display the phase for the two cases. According to the calculation, the perfect phase is $\sim -0.37\pi$ for the studied homojunction GaAs FIR detector, indicating that the phase of the mirror structure should approach -0.37π as close as possible. At wavelength shorter than 72 μm, the phase of the mirror structure is nearer to the resonant phase than that of the single doped layer. This explains that our present FIR/THz mirror structure performs well on the GaAs FIR detectors with operating wavelength of 60 μm [9]. Nevertheless, for longer operating wavelengths, we should adjust the structural parameters (thickness and doping concentration) of the mirror structure correspondingly to approach the resonant phase.

3.4. Experimental demonstration and discussion

To verify the above arguments on the energy flux and reflection, we have carried out experimental FIR/THz reflection and transmission measurements for the mirror structure. We note that the reflection of the mirror structure with optical entrance from a doped GaAs layer cannot be measured directly. The experimental measurements can only reveal the reflection/transmission of the mirror structure in air. However, if both the experimental reflection and transmission spectra of the mirror structure in air agree well with the theoretical results, the above analysis should be certainly true. This is due to the fact that all the calculation is determined by the same set of parameters. Fig. 5 shows both the experimental (filled squares) and theoretical (solid curves) FIR/THz reflection and transmission spectra for the GaAs mirror structure in air. The structure between 26 and 42 μm in the reflection spectrum is due to the TO phonon resonance of GaAs, corresponding to the non-transmission region in the transmission spectrum. It is clear that the calculated reflection and transmission spectra agree well with the experimental data throughout the measured FIR/THz region, demonstrating that all the above optical discussion about the GaAs FIR/THz mirror structure is reliable.

Finally, it should be noted that the present GaAs FIR/THz mirror structure is designed for specific GaAs homojunction FIR detectors. For other different GaAs-based multilayer FIR/THz devices, the mirror structure can simply be adjusted by changing the structural parameters (thickness and doping concentration) to

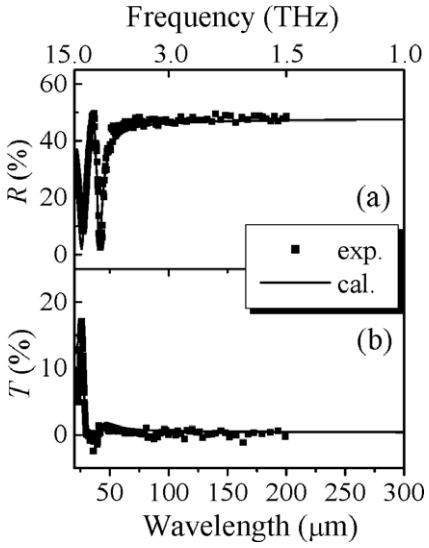

Fig. 5. Experimental (filled squares) and calculated (solid curves) FIR/THz reflection (a) and transmission (b) spectra of the doped/undoped GaAs FIR/THz mirror structure in air.

reach high optical reflectivity and well-matched phase, so that one can obtain high absorption probability in the FIR/THz device cavity. Therefore, such a doped/undoped GaAs mirror concept provides a way for the resonant cavity designs of GaAs-based FIR/THz detection/emission devices.

4. Conclusions

We investigate the transport and optical properties of doped/undoped GaAs FIR/THz mirror structures. Through variable magnetic field Hall and SdH measurements, the carrier concentration, mobility and two kinds of scattering time are obtained and analyzed. It is found that the ratio of classical to quantum scattering time is 1.79. Further analysis shows that the ionized impurity scattering is the dominant scattering mechanism at low temperatures for the GaAs FIR/THz mirror structures. The calculation of energy flux along the depth of the mirror structure shows that most of the absorption falls inside the highly doped bottom layer. Even though the reflection is lower than the traditional DBRs working in the near- and mid-infrared, the present GaAs FIR/THz mirror structure shows perfect enhancement effect in a wide FIR/THz region compared with a single doped layer. The calculated FIR/THz transmission and reflection spectra agree well with the experimental results for the mirror structure, demonstrating that all the optical analysis about GaAs FIR/THz mirror structure is reliable. We hope that the present doped/undoped GaAs mirror concept can be used in other GaAs-based FIR/THz devices, such as vertical-cavity surface emitting QCLs.

Acknowledgements

This work is supported in part by the Natural Science Foundation of China under Contract Nos. of 60006005, 10125416, 10304010 and 60576067, National Minister of Education PCSIRT and the Shanghai Key Projects for Basic Research of 03JC14082.

References

[1] D. Arnone, C. Ciesla, M. Pepper, Phys. World 13 (2000) 35.
[2] B.E. Cole, J.B. Williams, B.T. King, M.S. Sherwin, C.R. Stanley, Nature 410 (2001) 60.
[3] M.W. Werner, Infrared Phys. Technol. 35 (1994) 539.
[4] L. Suvillaret, F. Garet, J.L. Coutaz, Appl. Opt. 38 (1999) 409.
[5] G. Scalari, L. Ajili, J. Faist, H. Beere, E. Linfield, D. Ritchie, G. Davies, Appl. Phys. Lett. 82 (2003) 3165.
[6] W.Z. Shen, A.G.U. Perera, H.C. Liu, M. Buchanan, W.J. Schaff, Appl. Phys. Lett. 71 (1997) 2677.
[7] M.S. Ünlü, S. Strite, J. Appl. Phys. 78 (1995) 607.
[8] Y.H. Zhang, H.T. Luo, W.Z. Shen, Eur. J. Phys. Appl. Phys. 22 (2003) 165.
[9] Y.H. Zhang, H.T. Luo, W.Z. Shen, Appl. Phys. Lett. 82 (2003) 1129.
[10] R. Colombelli, K. Srinivasan, M. Troccoli, O. Painter, C.F. Gmachl, D.M. Tennant, A.M. Sergent, D.L. Sivco, A.Y. Cho, F. Capasso, Science 302 (2003) 1374.
[11] X.Y. Chen, W.Z. Shen, J. Phys., Condens. Matter 16 (2004) 997.
[12] W.A. Beck, J.R. Anderson, J. Appl. Phys. 62 (1987) 541.
[13] J. Antoszewski, J.M. Dell, L. Faraone, L.S. Tan, A. Raman, S.J. Chua, D.S. Holmes, J.R. Lindemuth, J.R. Meyer, Mater. Sci. Eng., B 44 (1997) 65.
[14] D.A. Anderson, N. Apsley, P. Davies, P.L. Giles, J. Appl. Phys. 58 (1985) 3059.
[15] S.B. Rafol, I.K. Sou, J.P. Faurie, J. Appl. Phys. 70 (1991) 4326.
[16] R.J. Justice, D.G. Seiler, W. Zawadzki, R.J. Koestner, M.W. Goodwin, M.A. Kinch, J. Vac. Sci. Technol., A 6 (1988) 2779.
[17] E.N. Adams, T.D. Holstein, J. Phys. Chem. Solids 10 (1959) 254.
[18] D. Jena, U.K. Mishra, Phys. Rev., B 66 (2002) 241307 (R).
[19] A. Gold, Phys. Rev., B 38 (1988) 10798.
[20] Z. Knittl, Optics of Thin Films, Wiley, London, 1976, p. 35.
[21] M.V. Klein, T.E. Furtak, Optics, 2nd ed., Wiley, New York, 1986, p. 295.
[22] J.S. Blakemore, J. Appl. Phys. 53 (1982) R123.